Variability of extragalactic X-ray jets on kiloparsec scales

Eileen Meyer (meyer@umbc.edu)
University of Maryland Baltimore County
Aamil Shaik
Department of Physics, University of Maryland Baltimore County
Yanbo Tang
Department of Statistical Sciences, University of Toronto
Nancy Reid
Department of Statistical Sciences, University of Toronto
Karthik Reddy
Department of Physics, University of Maryland Baltimore County
Peter Breiding
The William H. Miller III Department of Physics & Astronomy, Johns Hopkins University
Markos Georganopoulos
University of Maryland, Baltimore County
Marco Chiaberge
Space Telescope Science Institute
Eric Perlman
Florida Institute of Technology
Devon Clautice
Department of Physics and Space Sciences, Florida Institute of Technology
William Sparks
SETI Institute
Natalie DeNigris
University of Massachusetts Amherst
Max Trevor
University of Maryland

Article

Keywords:

Posted Date: June 14th, 2022

DOI: https://doi.org/10.21203/rs.3.rs-1654349/v1

Variability of extragalactic X-ray jets on kiloparsec scales

Eileen T. Meyer*[1], Aamil Shaik[1], Yanbo Tang[2], Nancy Reid[2], Karthik Reddy[1], Peter Breiding[1,3], Markos Georganopoulos[1], Marco Chiaberge[3,4], Eric Perlman[5], Devon Clautice[5], William Sparks[6,7], Natalie DeNigris[1,8], Max Trevor[1,9]

[1]*Department of Physics, University of Maryland Baltimore County, 1000 Hilltop Circle Baltimore, MD 21250, USA*

[2]*Department of Statistical Sciences, University of Toronto, 700 University Avenue, Toronto ON M5G 1Z5, Canada*

[3]*The William H. Miller III Department of Physics & Astronomy, Johns Hopkins University, Baltimore, MD 21218, USA*

[4]*Space Telescope Science Institute for the European Space Agency, ESA Office, 3700 San Martin Drive, Baltimore, MD 21218, USA*

[5]*Department of Physics and Space Sciences, Florida Institute of Technology, 150 W. University Boulevard, Melbourne, FL 32901, USA*

[6]*SETI Institute, 339 Bernardo Ave. Suite 200, Mountain View, CA 94043*

[7]*Space Telescope Science Institute, 3700 San Martin Drive, Baltimore, MD 21218, USA*

[8]*UM Amherst*

[9]*University of Maryland, College Park, MD 20742, USA*

Super-massive black holes residing at the centres of galaxies can launch powerful radio-emitting plasma jets which reach scales of hundreds of thousands of light-years, well be-

yond their host galaxies.[1] The advent of *Chandra*, the only X-ray observatory capable of sub-arcsecond-scale imaging, has lead to the surprising discovery of strong X-ray emission from radio jets on these scales.[2–4] The origin of this X-ray emission, which appears as a second spectral component from that of the radio emission, has been debated for over two decades.[5–9] The most commonly assumed mechanism is inverse Compton upscattering of the Cosmic Microwave Background (IC-CMB) by very low-energy electrons in a still highly relativistic jet.[10,11] Under this mechanism no variability in the X-ray emission is expected. Here we report the detection of X-ray variability in the large-scale jet population, using a novel statistical analysis of 53 jets with multiple *Chandra* observations. Individually 13/53 jets have at least one feature which is variable at the $p<0.05$ level. Taken as a population, we find that the distribution of p-values from a Poisson model is strongly inconsistent with steady emission, with a global p-value of 1.96×10^{-4} under a Kolmogorov-Smirnov test against the expected Uniform (0,1) distribution. The inconsistency significantly increases when we exclude core-dominated quasars at high redshift. These results strongly imply that the dominant mechanism of X-ray production in kpc-scale jets is synchrotron emission by a second population of electrons reaching multi-TeV energies. X-ray variability on the time-scale of months to a few years implies extremely small emitting volumes much smaller than the cross-section of the jet.

Main

Our analysis sample comprises nearly all known X-ray jets imaged more than once by the *Chandra* Advanced CCD Imaging Spectrometer (ACIS) instrument, a total of 53 sources. The average number of observations per source in our sample is 3.4, with a mean spacing of 2.6 years. More than half (30) have been observed only twice, while a small number (6) have more than five distinct observations. We have excluded two sources (3C 305 and 3C 171) where the X-ray emission associated to the radio jet has been attributed to jet-drive gas[12,13], as well as the two most deeply observed jets in the known population, M87 and Centaurus A. The X-ray emission in these latter sources is consistent with the falling tail of the radio-optical synchrotron spectrum[14–16]. Both M87 and Centaurus A have been far more deeply and frequently observed than typical of the remaining sample (with 50 and 43 distinct observations, respectively), and this is likely one of the reasons that X-ray variability has been reported in both cases[17–19]. With the exception of the source known as Pictor A, variability has not been reported for any other source in our sample of 53. Previously, a knot in the jet of Pictor A was seen to fade over a timescale of a few years[18] with a reported significance of 3.4σ, and potential low-level variability has been reported for the terminal hotspot[19]. Unlike the jets of M87 and Centaurus A, however, the X-ray emission in Pictor A is clearly from a second emission component[20], distinct from the radio-optical and is thus retained in our sample.

For each X-ray jet, we produced a deep co-added X-ray image by aligning and stacking all available epochs. We obtained complimentary radio-wavelength images at matching or better resolution, predominantly using archival data from the Very Large Array (VLA). We aligned and

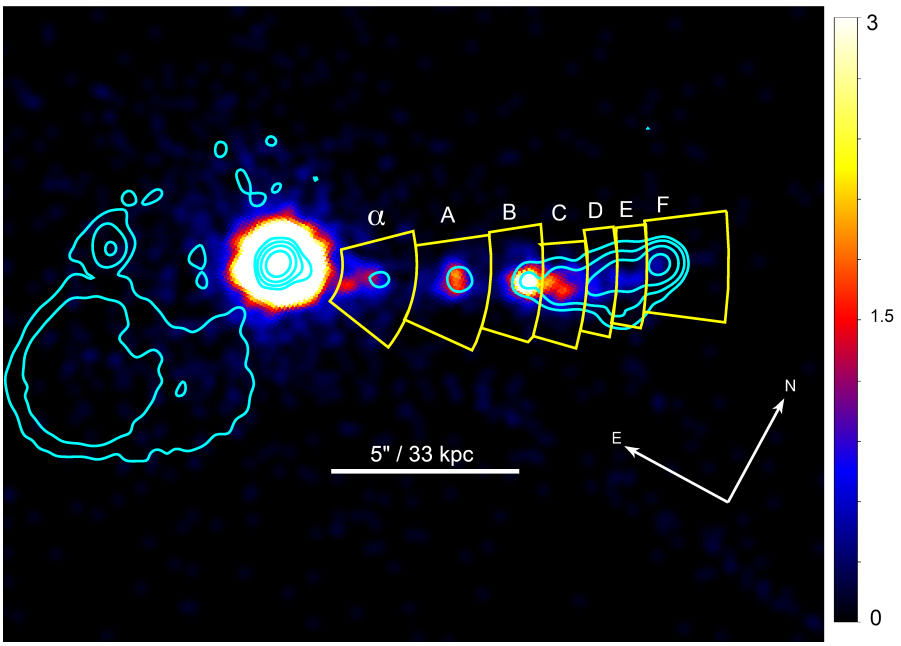

Figure 1 | A *Chandra* X-ray image (0.3-7 keV) of PKS 1136-135, one of the 53 X-ray emitting jets in our sample. The color scale is in counts and the image has been lightly smoothed (Gaussian kernel of width 3 pixels). The brightest region, known as the 'core' of the jet, is the location of the galaxy center and black hole. Overlaid in cyan are contour lines from a radio image at 5 GHz (the counter-jet radio lobe is visible to the left of the core). The regions outlined in yellow and labeled are individual emitting regions (knots) identified through a cross-comparison of the radio and X-ray structure.

overlaid the radio and X-ray images of the jet to identify distinct compact zones of emission, referred to as knots (see Figure 1). At these scales, individual knots are causally independent (the minimum knot-to-knot spacing among all jets is 650 ly de-projected, and on average it is nearly 200.000 ly). Our analysis assesses variability for individual knot regions rather than the entire extended jet due to the potential for independent and random variations along the jet to cancel out and reduce the statistical power of our test.

For each knot we define a consistent geometric area (knot region) for extracting the total X-ray counts from each epoch, as depicted for the source PKS 1136-135 in Figure 1. A corresponding

larger region is used to estimate the counts from background emission. Further details of the data analysis and preparation are given in Methods and Supplemental Information, and a full description of the source and region properties and measurements are given in the Supplementary Information Tables $1-4$.

Our likelihood function is a straightforward application of Poisson statistics (see Methods), with a null hypothesis of a steady source rate for each individual knot region, taking into account a varying background. For each knot, the observed source and background counts for all individual observations (epochs), along with the corresponding exposure (in units of area $\times$ time) in the respective regions for that epoch are the data. We compute for each knot a *p*-value for the test of the the null hypothesis of a steady source rate, and a maximum-likelihood estimate of the mean count rate for the knot, $\bar{\mu}$. If the X-ray emission from the tested regions are non-variable, these single-region *p*-values for the full sample of 155 knot regions are expected to follow a $U(0,1)$ distribution.

Out of the full sample of 155 regions tested, 18 (12%) have *p*-values less than 0.05, suggesting significant variability in the intrinsic source rate. However, in a sample context a certain number of low *p*-values may occur by chance. We compare all 155 single-region *p*-values to a $U(0,1)$ distribution using a one-sided Kolmogorov-Smirnov (KS) test, and found a significant excess of low *p*-values. The *p*-value for testing the uniformity of the single-region *p*-values by the KS statistic is 0.000196.[1] This clearly indicates that the observations are not consistent with a

[1]To avoid confusion, we hereafter refer to the *p*-values from the maximum likelihood function for a single region as 'single-region' *p*-values, and the *p*-values associated with the KS-test of the entire distribution of the latter as the 'global' or 'KS-test' *p*-value.

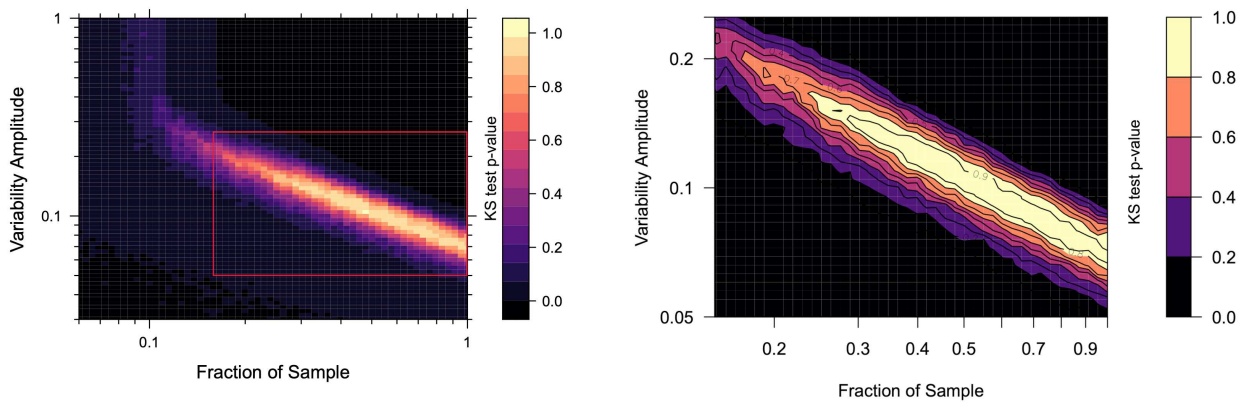

Figure 2 | Level plots showing the *p*-value for a KS test comparing simulated data sets to our observed single-region *p*-value distribution. Here we have varied the simulated fraction of the population which is variable (x-axis) and the amplitude of the variability for that subset (y-axis). Higher KS-test *p*-values (lighter colors) indicate closer agreement with the observed data. At left we show the full results of all simulations, while at right we show a filled contour plot corresponding to the region outlined in red at left. While there is a degeneracy between the amplitude of variability and the variable fraction, the simulations imply at least 30% of the population is variable and that the typical scale of the variability is on the order of 10% compared to the mean.

universal constant source rate.

Based on the above statistic alone, it is unclear whether the signature of variability reflects consistent lower-amplitude variations throughout the sample or if only a subset exhibits higher-amplitude variability. Assuming that the known population of X-ray emitting jets may be a mixture of truly steady and variable jets, for an observed single-region p-value distribution there is a trade-off between the fraction of the sample which is intrinsically variable and the amplitude of that variability. To illustrate this and to estimate roughly the scale of the variability in the population as a whole, we performed Monte Carlo simulations using the real average exposure values for the knot regions as well as their estimated mean count rates $\bar{\mu}$. We used a simple model of variability, of two

epochs with a fixed percentage variance relative to mean, and use a KS test to compare a simulated single-region p-value distribution (n=10.000) with our real distribution. The resulting p-values from the KS test comparisons are displayed in Figure 2 as a two-dimensional color map with axes of variability amplitude (percent relative to mean rate $\bar{\mu}$) versus the fraction of the sample which is variable versus steady. Lighter colors (indicating sample KS-test p-values closer to 1) show the simulations most resembling the data. As shown, high-amplitude variability (over $\sim$25%, relative to $\bar{\mu}$) is disfavoured, but there is some degeneracy below this, running up to the possibility of low-level (few-percent-scale) variability throughout the population.

Variability in the X-ray emission from large-scale jets on timescales of a few months $-$ years is not compatible with the IC/CMB mechanism: the CMB is completely steady, and the electrons upscattering it are very low energy (Lorentz factor $\gamma \sim 100 - 1000$), with extremely long cooling timescales, many orders of magnitude longer than the light-crossing time for the jet.[18,21] However, a synchrotron origin is compatible with short-timescale variability,[18] as the X-rays must be emitted by very energetic multi-TeV energy electrons, where the cooling timescale is accordingly much shorter. Combined with a very small emitting volume (on the order of light-months), it is possible to produce the observed variability. We therefore suggest that this variability is strong evidence that the X-ray emission in these jets is more likely to be synchrotron radiation from a very high-energy electron population population. It is notable that the required small volumes are, however, in conflict with the typical assumption of particle acceleration which is distributed throughout the jet cross-section[22] and pose significant challenges to current theoretical models.

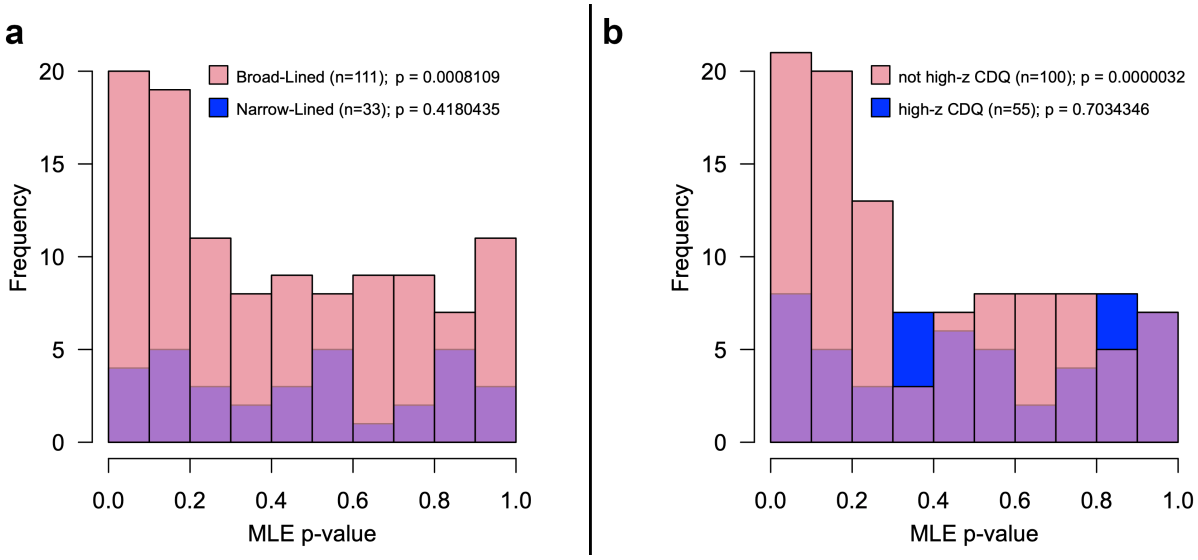

Figure 3 | **Histograms of the single-region *p*-values.** The full sample of 155 knot regions is divided into two sub-populations based on host AGN or jet/region attributes. Panel (a) shows broad-lined AGN (red) versus narrow-lined (blue). The narrow-lined sources appear consistent with a steady source rate, unlike broad-lined sources. In panel (b) we see that the sub-set of sources which excludes core-dominated quasars at high redshift shows a single-region *p*-value distribution which is more discrepant from a $U(0,1)$ distribution than the full sample. This implies that high-redshift core-dominated quasars could represent a true non-variable population, in keeping with theoretical expectations. (See Extended Data Table 2 for the results of all examined sub-populations.)

Our sample exhibits considerable variety in terms of jet and knot region characteristics such as jet orientation, length, redshift, knot distance from the central engine, spectral type of the host nucleus (broad or narrow/absent optical emission lines), etc. The sample also covers several orders of magnitude in jet power (as proxied by the low-frequency radio luminosity). To test if any particular source characteristics were more associated with variability than others, we split the sample into two subsets and re-ran the one-sided KS test of the single-region *p*-value distribution against a $U(0,1)$ distribution for each subset. The results are summarised in Table 1 and Extended Data Table 2, where we give the tested characteristic, the sub-sample definitions and size, and the resulting KS-test *p*-values. For subsets where the KS-test *p*-value is lower than that of the full sample, the final column in these tables gives a percentage which is the percent probability of obtaining the lower KS-test *p*-value purely by chance for a subselection of size n from the full parent population (i.e., the percentile). Histograms depicting the *p*-value distribution for two of subselections are shown in Figure 3.

We found that 5 subselections (out of 12 total) yield a sample with a lower KS-test *p*-value than the full population, with percentiles ranging from $0.21-7.33\%$. We interpret the combination of a lowered *p*-value with a low percentile for one subset to mean that the compliment subset either contains more steady jets relative to the subset with a lowered KS-test *p*-value, or preferentially displays variability below our detection sensitivity for those regions, which varies due to factors like the relative level of background radiation and intrinsic brightness.

Significantly lower KS-test *p*-values are found for the sub-samples comprised of *(i)* regions

Table 1 | Select results of sub-sample KS-tests against $U(0,1)$ distribution

Characteristic	Subset	n	Definition	KS-test $p-$value	Percentile
Core dist.	Far	83	$d > 5''$	0.000033	2.20%
	Near	72	$d < 5''$	0.29	
Jet Angle	High	78	$\theta >= 15.5$	0.00012	6.18%
	Low	77	$\theta < 15.5$	0.12	
Redshift	low	75	$z < 0.6$	0.0000035	0.36%
	high	80	$z >= 0.6$	0.15	
Jet class	not CDQ	81	...	0.00015	7.33%
	CDQ	74		0.13	
Jet class + redshift	not high-z CDQ	100	...	0.0000032	0.21%
	high-z CDQ	55		0.70	

more than $5''$ from the bright central core, *(ii)* low-redshift sources (z <0.6), *(iii)* sources with larger jet angles to the line-of-sight ($\theta > 15.5°$), and *(iv)* jets classed as anything other than core-dominated quasars (that is, removing core-dominated quasars significantly increased the signal of variability, suggesting they could be less variable).

For case *(i)* the improvement in the variability signal by removing knots very near to bright cores is not surprising. Our simulation above as well as a simple histogram of the percent variation from mean for all regions (Extended Data Figure 4) strongly suggests that the typical variability level in the population is at the few to tens of percent level (as opposed to large orders-of-magnitude flares). Variability at this level may not be detectable in some test regions due to shorter exposures, intrinsically low source flux, relatively high levels of background, or any combination of these factors. These factors generally produce observations with a low number of total counts attributed to the source, which sets a lower limit on the amplitude of variability we can detect. We call this limit the sensitivity threshold (ST), and for high-background regions (common for knots near the

bright base of the jet or core), the ST may be well above the typical source variability amplitude, while this is less likely to be the case for regions with low background or encompassing relatively brighter knots. A further discussion of ST and its estimation for our regions is in the Supplemental Information.

In all the other cases of subsets with a significantly lower KS-test *p*-value the compliment subset (with a higher *p*-value) are source populations where the likelihood of steady IC/CMB emission being dominant is supported on theoretical grounds. For all such 'excluded' populations we cannot reject the null hypothesis that the emission is non-variable. Regarding case *(ii)*, because the CMB energy density increases dramatically with redshift as $(1+z)^4$, there has long been an expectation that the IC/CMB mechanism of X-ray production would increasingly dominate with redshift, leading to a strong correlation between X-ray/radio flux ratio and redshift in resolved jets[23] and an enhancement in the total X-ray emission even for unresolved jets.[24] Until recently, the severe lack of high-redshift sources among the known X-ray jets (with only a handful above $z \sim 3$) made it difficult to determine whether the lack of an observed correlation was a contradiction to this expectation or merely a reflection of wide scatter in the intrinsic X-ray/radio flux ratio and/or inadequate sampling.[4,7] In recent years, however, several very high-redshift X-ray jets and jet candidates have been identified, all of which show very high X-ray/radio flux ratios strongly suggesting an IC/CMB origin.[25–27] Studies of high-redshift quasars also show significant ($> 50\%$) total X-ray flux enhancements at high redshifts ($z > 3$), which has been attributed to IC/CMB emission in unresolved large-scale jets.[24] Our results alongside these recent discoveries suggest a gradual change in the jet population, from synchrotron-dominated at lower redshift, giving way to

increasing IC/CMB dominance in the population at high redshift. While a small handful of jets at lower-redshift, under favorable conditions, may have X-ray emission produced by IC/CMB[28], recent observations with the *Fermi* gamma-ray observatory also disfavor an IC/CMB origin for many low to moderate-redshift jets.[8,29]

In the final two cases the excluded populations are core-dominated quasars and (with significant overlap of $\sim$90%) sources with a small estimated angle to the line-of-sight. This is also in keeping with theoretical expectations as inverse Compton emission is more sensitive to the increased Doppler boosting of the relativistic jet with decreasing angle to the line-of-sight[30,31]. When we make a double selection, excluding only the 47 high-redshift core-dominated quasars, the one-sided KS-test *p*-value against a $U(0,1)$ distribution of the remaining sample decreases to 0.0000032, with a 0.21% probability of occurring by chance.

In addition to the results presented here, two nearby and very well-known X-ray jets have been extensively and deeply studied with the *Chandra* observatory, moreso than any other jets. These are Centaurus A and M87. In comparison to our sample, these low-redshift jets have far more extensive and deeper observations, with 43 and 50 distinct observations totalling 1129 and 460 ks of total time on source, respectively (the median total time for our sample is 63 ks in comparison). Prior works have already extensively described their characteristics, including the unprecedented (and unrepeated) X-ray flare from knot HST-1 in M87, where the X-ray flux increased by a factor of over 50 during the mid-2000s, before fading back to its prior level[32]. The variability in Centaurus A, by contrast, appears as a gradual dimming consistent with adiabatic expansion.[33] In terms of

spectrum, the unusually deep observations of M87 and Cen A make it clear that the X-ray emission is from the high-energy falling tail of the radio synchrotron component, and the X-ray variability is thus consistent with this picture. Since we are mainly interested in testing the inverse Compton scenario for jets in which the X-rays are or might be from a second emission component, we do not include these sources in our analysis. The one other jet previously reported as variable is Pictor A. In contrast to M87 and Cen A, the X-ray emission is clearly from a distinct second spectral component[20], and previous works have suggested variability in both the jet and hotspot.[18,19] In this work we confirm that Pictor A is strongly variable and find that five of the nine regions in the jet, including the hotspot, are variable at the p <0.05 level, and the mean of the absolute value of the percent variation from $\bar{\mu}$ is 18%.

The fact that all three of the most deeply observed X-ray show variability lends support to the population-based findings in this work. For completeness and as a check of our methods, we also analysed the two X-ray jets previously excluded due to the X-ray emission being from surrounding gas (3C 305 and 3C 171). In these cases no variability is expected due to the scale of the X-ray emission. Indeed, in our analysis none of the regions give single-region p-values less than 0.18 and thus all are consistent with a steady source rate.

The short timescales of X-ray variability observed in this and prior works implies that the emitting regions responsible are much smaller that the width of the jet. By the light crossing time argument a flare event on the order of a year cannot occur in a region larger than a few parsecs, vastly smaller than the typical resolved cross-section in the radio which is of the order

of a kpc or more. This requires extremely localised particle acceleration, more easily achieved through magnetic reconnection than through the usually assumed shock acceleration.[34] At present we lack a clear understanding of particle acceleration in extragalactic jets. Future theoretical work must take into account the requirements of short-timescale X-ray variability and the implied multi-TeV energy electrons produced on scales of hundreds of thousands of light years from the central engine.

1. Blandford, R., Meier, D. & Readhead, A. Relativistic Jets from Active Galactic Nuclei. *Annual Review of Astronomy and Astrophysics* **57**, 467–509 (2019). 1812.06025.

2. Chartas, G. *et al.* The Chandra X-Ray Observatory Resolves the X-Ray Morphology and Spectra of a Jet in PKS 0637-752. *The Astrophysical Journal* **542**, 655–666 (2000). astro-ph/0005227.

3. Sambruna, R. M. *et al.* A Survey of Extended Radio Jets with Chandra and the Hubble Space Telescope. *The Astrophysical Journal* **608**, 698–720 (2004). astro-ph/0401475.

4. Marshall, H. L. *et al.* An X-Ray Imaging Survey of Quasar Jets: The Complete Survey. *The Astrophysical Journal* **856**, 66 (2018). 1802.04714.

5. Schwartz, D. A. *et al.* Chandra Discovery of a 100 kiloparsec X-Ray Jet in PKS 0637-752. *The Astrophysical Journal Letters* **540**, 69–72 (2000). astro-ph/0005255.

6. Hardcastle, M. J. Testing the beamed inverse-Compton model for jet X-ray emission: velocity structure and deceleration. *Monthly Notices of the Royal Astronomical Society* **366**, 1465–

1474 (2006). astro-ph/0511511.

7. Marshall, H. L. *et al.* An X-ray Imaging Survey of Quasar Jets: Testing the Inverse Compton Model. *ApJS* **193**, 15 (2011). 1101.5822.

8. Breiding, P. *et al.* Fermi Non-detections of Four X-Ray Jet Sources and Implications for the IC/CMB Mechanism. *The Astrophysical Journal* **849**, 95 (2017). 1710.04250.

9. Reddy, K., Georganopoulos, M. & Meyer, E. T. X-Ray-to-radio Offset Inference from Low-count X-Ray Jets. *ApJS* **253**, 37 (2021). 2101.02024.

10. Tavecchio, F., Maraschi, L., Sambruna, R. M. & Urry, C. M. The X-Ray Jet of PKS 0637-752: Inverse Compton Radiation from the Cosmic Microwave Background? *The Astrophysical Journal Letters* **544**, L23–L26 (2000). astro-ph/0007441.

11. Celotti, A., Ghisellini, G. & Chiaberge, M. Large-scale jets in active galactic nuclei: multi-wavelength mapping. *Monthly Notices of the Royal Astronomical Society* **321**, L1–L5 (2001). astro-ph/0008021.

12. Hardcastle, M. J. *et al.* The nature of the jet-driven outflow in the radio galaxy 3C 305. *Monthly Notices of the Royal Astronomical Society* **424**, 1774–1789 (2012). 1205.0962.

13. Hardcastle, M. J., Massaro, F. & Harris, D. E. X-ray emission from the extended emission-line region of the powerful radio galaxy 3C171. *Monthly Notices of the Royal Astronomical Society* **401**, 2697–2705 (2010). 0910.1060.

14. Feigelson, E. D. *et al.* The X-ray structure of Centaurus A. *The Astrophysical Journal* **251**, 31–51 (1981).

15. Kraft, R. P. *et al.* Chandra Observations of the X-Ray Jet in Centaurus A. *The Astrophysical Journal* **569**, 54–71 (2002). astro-ph/0111340.

16. Wilson, A. S., Young, A. J. & Shopbell, P. L. Chandra Observations of Cygnus A: Magnetic Field Strengths in the Hot Spots of a Radio Galaxy. *The Astrophysical Journal Letters* **544**, L27–L30 (2000). astro-ph/0009308.

17. Harris, D. E. *et al.* Flaring X-Ray Emission from HST-1, a Knot in the M87 Jet. *The Astrophysical Journal Letters* **586**, L41–L44 (2003). astro-ph/0302270.

18. Marshall, H. L. *et al.* A Flare in the Jet of Pictor A. *The Astrophysical Journal Letters* **714**, L213–L216 (2010). 1004.0191.

19. Hardcastle, M. J. *et al.* Deep Chandra observations of Pictor A. *Monthly Notices of the Royal Astronomical Society* **455**, 3526–3545 (2016). 1510.08392.

20. Hardcastle, M. J. & Croston, J. H. The Chandra view of extended X-ray emission from Pictor A. *Monthly Notices of the Royal Astronomical Society* **363**, 649–660 (2005). astro-ph/0507694.

21. Georganopoulos, M., Kazanas, D., Perlman, E. & Stecker, F. W. Bulk Comptonization of the Cosmic Microwave Background by Extragalactic Jets as a Probe of Their Matter Content. *The Astrophysical Journal* **625**, 656–666 (2005). astro-ph/0502201.

22. Alves, E. P., Zrake, J. & Fiuza, F. Efficient Nonthermal Particle Acceleration by the Kink Instability in Relativistic Jets. **121**, 245101 (2018). 1810.05154.

23. Marshall, H. L. *et al.* A Chandra Survey of Quasar Jets: First Results. *ApJS* **156**, 13–33 (2005). astro-ph/0409566.

24. Zhu, S. F., Brandt, W. N., Wu, J., Garmire, G. P. & Miller, B. P. Investigating the X-ray enhancements of highly radio-loud quasars at z ¿ 4. *Monthly Notices of the Royal Astronomical Society* **482**, 2016–2038 (2019). 1810.06572.

25. Worrall, D. M. *et al.* Inverse-Compton scattering in the resolved jet of the high-redshift quasar PKS J1421-0643. *Monthly Notices of the Royal Astronomical Society* **497**, 988–1000 (2020). 2007.03536.

26. Schwartz, D. A. *et al.* Two Candidate High-redshift X-Ray Jets without Coincident Radio Jets. *The Astrophysical Journal* **904**, 57 (2020). 2010.06535.

27. Ighina, L. *et al.* Direct observation of an extended X-ray jet at z=6.1. *arXiv e-prints* arXiv:2111.08632 (2021). 2111.08632.

28. Meyer, E. T. *et al.* The Origin of the X-Ray Emission in Two Well-aligned Extragalactic Jets: The Case for IC/CMB. *The Astrophysical Journal Letters* **883**, L2 (2019). 1908.07139.

29. Breiding, P., Meyer, E. T. & Georganopoulos, M. A Multi-Wavelength Study of Multiple Spectral Component Jets in AGN: Testing the IC/CMB Model for the Large-Scale-Jet X-ray Emission. *submitted to MNRAS* (2022).

30. Dermer, C. D. On the Beaming Statistics of Gamma-Ray Sources. *The Astrophysical Journal Letters* **446**, L63 (1995).

31. Georganopoulos, M., Kirk, J. G. & Mastichiadis, A. The Beaming Pattern and Spectrum of Radiation from Inverse Compton Scattering in Blazars. *The Astrophysical Journal* **561**, 111–117 (2001). astro-ph/0107152.

32. Harris, D. E., Cheung, C. C., Stawarz, Ł., Biretta, J. A. & Perlman, E. S. Variability Timescales in the M87 Jet: Signatures of E ^{2} Losses, Discovery of a Quasi Period in HST-1, and the Site of TeV Flaring. *The Astrophysical Journal* **699**, 305–314 (2009). 0904.3925.

33. Snios, B. *et al.* Variability and Proper Motion of X-Ray Knots in the Jet of Centaurus A. *The Astrophysical Journal* **871**, 248 (2019). 1901.00509.

34. Giannios, D., Uzdensky, D. A. & Begelman, M. C. Fast TeV variability in blazars: jets in a jet. *Monthly Notices of the Royal Astronomical Society* **395**, L29–L33 (2009). 0901.1877.

Methods

Initial Chandra Data Analysis & Imaging The initial list of known X-ray jets was taken from the XJET online database[1] and from a search of the literature, a total of 199 jets. A comprehensive catalog of known X-ray jets to date can be found in the recent ATLAS-X publication[2]. For the 55 multiply-observed sources in our sample, we downloaded all available observations taken with *Chandra*'s Advanced CCD Imaging Spectrometer (ACIS[3]). Supplemental Information Table 1 lists the names and properties of the sample of 55 jets, and a complete list of the *Chandra* observations used can be found in the Supplemental Information Table 2.

For the X-ray data analysis, we used `CIAO`[4] 4.12 and `CALDB`[5] 4.9.2 . Each observation was first reprocessed using the `chandra_repro` command. We applied a standard energy filter including only events from 0.4-8 keV. Excluding all bright sources in the field of view, we extracted the background counts and used the `lc_clean` task to examine the data for background flares with a good time interval (GTI) bin time of 259.28 s and cutting intervals with rates more than 2σ from the mean count rate. The total exposure times before and after filtering is given in Supplemental Information Table 2.

We used this filtered data to produce initial sub-pixel images centered on the core of the X-ray jet for each observation, downsizing by a factor of 5 (a pixel scale of $0.0984''$). We then co-added all epochs in order to make a deep sub-pixel image for comparison to the radio imaging and to identify knot regions. Before co-adding, we corrected for pointing offsets by aligning the point-source-like jet core in all exposures. To do so we manually calculated the offsets between

the earliest available observation and all subsequent observations using the centroid task in CIAO. Using these offsets, we corrected the aspect solution and reprojected all observations to match the reference epoch. We then repeated our filtering and sub-pixel binning process on the reprojected data to create a reprojected subpixel image for each epoch. These were finally merged using the dmmerge to produce the deepest combined subpixel image of the X-ray jet for morphological study. For sources with observations in both the FAINT and VFAINT modes, which can not be merged using CIAO's dmmerge command, we used a Python script to manually sum all the counts for each subpixel in the matched two-dimensional image frame.

Radio observations Where possible, we utilised radio imaging of comparable resolution to *Chandra* ($0.2" - 0.7"$). Most radio images (32) were newly reduced for this work from archival Very Large Array (VLA), Atacama Large Millimeter/sub-millimeter Array (ALMA), or Australia Telescope Compact Array (ATCA) observations (26, 3, and 3 sources, respectively). For these we followed a standard procedure of calibrating the visibilities using the Common Astronomy Software Applications[6] (CASA) software before deconvolving the image using the CASA task clean with a Briggs (weighting) parameter of 0.5. Several rounds of self-calibration were generally used to improve the image quality. For the remaining 22 sources we used pre-existing publicly available radio images from the NASA Extragalactic Database[7] (NED, 4 sources), the XJET catalog (5 sources), or the NRAO VLA Archive Survey (NVAS, 13 sources). A complete table of the radio observations used can be found in Extended Data Table 3. Contour lines (showing level of emission) corresponding to the radio imaging were overlaid on our co-added X-ray image as shown in Figure1, and we identified all distinct knots and hotspots for analysis. We ignored radio knots

which were within and visually indistinguishable from the X-ray core and those which had no visible X-ray emission. We note that while it is now well established that radio and X-ray knots do not always perfectly coincide[2], the inferred offsets from radio to X-ray are small, with most being $<0.2''$. This is smaller than the *Chandra*/ACIS pixel scale and much smaller than our region sizes.

X-ray Spectral Analysis and Measurement We defined polygon regions for each knot or hotspot, being careful to avoid overlap and to encompass fully each individual emission region. For knots close to the bright central X-ray core, we used an annulus region to define simultaneously the knot (a slice of the annulus centered on the core) and its matched background (the remainder of the annulus). This is depicted in Extended Data Figure 5 for source PKS 1928+738. In cases where a readout streak was present, this was excised proportionately from the annulus background. For knots and hotspots far from the core, a simple polygon encompassing the feature was used to extract the source counts, and a large representative region far from any source was used to estimate the background. For the 155 total jet features analysed, 93 are annulus-type regions. For jets with more than one knot region, we also defined a region encompassing the entire jet for spectral analysis. For each observation, we extracted the counts using the CIAO `specextract` command from every region and its associated background, including the total jet region.

In order to estimate the total jet spectral index we used `sherpa` to fit the counts extracted from the total jet region with an absorbed power-law model using the galactic Hydrogen column density (nH) values from the HI4PI survey.[8] In the common cases of relatively low background, it was simply subtracted. For annulus-type regions we used a second absorbed power-law to model

the background (dominated by the core). In a few cases, a thermal component in the background model was required to improve the spectral fit. These details are noted in Supplemental Information Table 1.

The total photon counts (per epoch) in our knot regions ranged from 1 to 2156 with a median value of 38. In most cases, the photon statistics for individual knots are too low to allow us to effectively constrain the X-ray spectral index (Γ) for that region alone. We attempted a spectral fit for each of the 155 regions in our sample using `sherpa`. Of the 52 sources in our sample, 11 sources have a single knot region of interest and thus no distinction between the spectral fit of the knot and the overall jet. The remaining 41 sources each have knot regions of interest within the jet, totalling up to 144 regions. In these cases, we compared the spectral fits we obtained from fitting the emission from all the knots together (a 'total jet' region) to the spectral fits for each individual knot. Of these, we find that the total jet Γ is within 1 σ of the knot value of Γ for 110 regions and is within 2 σ for 21 regions. The remaining 13 knot regions either have poor spectral fits (reduced $\chi^2 > 1$) or do not have enough counts for the fit to converge. Given this, we used the Γ value from the fit to the entire jet region when generating the exposure maps for each source. We input this into the CIAO task `make_instmap_weights` to create a weights file for each observing epoch over our energy range of 0.4 to 8 keV. We then used the `fluximage` command to generate exposure maps. We used a python script to extract the raw counts and total exposures from our previously generated reprojected image and exposure map, respectively, for both the knot region and its associated background at every epoch.

Recent work has shown that X-ray emission from jet knots are unresolved in *Chandra* observations, and we accordingly treat them as point sources.[2] Since the source regions are generally small (on the order of arcseconds), the measured number of photons from the source will be less than the total falling on the detector due to the limited size of the region. The encircled counts fraction (ECF) is simply the ratio of the counts falling within the finite region compared to the total over the full detector. While the ECF is generally similar across epochs, it does have slightly different values due to changes in the PSF and/or changes in the detector position of the feature. We have thus used simulated PSFs from the ATLAS-X catalog of X-ray jets and our region files to measure the ECF in each epoch. These values are tabulated in Supplemental Information Table 4.

Statistical Analysis Method Let (X_i, Y_i), $i = 1, \ldots, n$, be the background and source measurement, respectively for a given knot, where i iterates over all exposures (epochs) and (a_i, b_i) is the exposure (as measured in time multiplied by area) for the background and source measurement respectively. In addition, the source region will have an associated encircled counts fraction f_i. The encircled counts fraction and exposures are assumed to have negligible measurement error. Consider the following joint model for the observations X_i and Y_i

$$X_i \sim \text{Poisson}(a_i\beta_i), \quad Y_i \sim \text{Poisson}(b_i\beta_i + b_i f_i \mu_i),$$

where β_i is the rate of background activity and μ_i is the rate of the source radiation for the i-th observation. We are interesting in testing the null hypothesis $H_0 : \mu_1 = \cdots = \mu_n$; the hypothesis

that the source rates do not vary. The log-likelihood function is

$$l(\mu, \beta; X, Y) = \sum_{i=1}^{n} \left\{ X_i \log(a_i \beta_i) - a_i \beta_i + Y_i \log(b_i \beta_i + b_i f_i \mu_i) - b_i \beta_i - b_i f_i \mu_i \right\},$$

where μ, β, X, Y are the vectorized version of the parameters and observations. In this section, we provide the necessary components for the construction of a directional test statistic, which has been found to be highly accurate in the small sample setting. The definitions and theoretical details can be found in a previous publication[9], and numerous experiments demonstrating the numerical accuracy of this method are contained within the referenced work. The unconstrained maximum likelihood estimators (MLEs) for μ_i and β_i are

$$\hat{\beta}_i = \frac{X_i}{a_i} \quad \hat{\mu}_i = \frac{Y_i}{f_i b_i} - \frac{\hat{\beta}_i}{f_i}, \quad i = 1, \ldots, n.$$

The constrained MLEs under H_0, $(\hat{\mu}_0, \hat{\beta}_{0,1}, \ldots, \hat{\beta}_{0,n})$, are obtained by numerically maximizing

$$l(\mu^\star, \beta; X, Y) = \sum_{i=1}^{n} \left\{ X_i \log(a_i \beta_i) - a_i \beta_i + Y_i \log(b_i \beta_i + f_i b_i \mu^\star) - b_i \beta_i - f_i b_i \mu^\star \right\},$$

where $\mu^\star$ is a scalar variable.

The tangent exponential family approximation to the likelihood is

$$l(\phi(\theta); s(t)) = \sum_{i=1}^{n} \Big[-(1-t)\phi_i \left\{ X_i - a_i \exp(\hat{\phi}_{0,i}) \right\} - (1-t)\phi_{n+i} \left\{ Y_i - b_i \exp(\hat{\phi}_{0,n+i}) \right\}$$
$$+ X_i\{\log(a_i) + \phi_i\} - a_i \exp(\phi_i) + Y_i\{\log(b_i) + \phi_{n+i}\} - b_i \exp(\phi_{n+i}) \Big], \quad (1)$$

where ϕ are the canonical parameters in the Poisson model:

$$\phi(\mu, \beta) = \begin{cases} \log(\beta_i) \text{ for } i = 1, \ldots, n, \\ \\ \log(f_{i-n}\mu_{i-n} + \beta_{i-n}) \text{ for } i = n+1, \ldots, 2n. \end{cases}$$

$s(t)$, the line linking the score at the MLE ($\hat{\phi}$) and the score at the constrained MLE under the null hypothesis ($\hat{\phi}_0$), under the canonical parameterization, is

$$s(t) = \begin{cases} -(1-t)(X_i - a_i \exp(\hat{\phi}_{0,i})) \text{ for } i = 1, \ldots, n \\ \\ -(1-t)(Y_{i-n} - b_{i-n} \exp(\hat{\phi}_{0,i})) \text{ for } i = n+1, \ldots, 2n. \end{cases}$$

The *p*-value for testing H_0, based on observations (X, Y) is obtained by the following ratio of integrals:

$$\frac{\int_1^{t_{\max}} h_0\{s(t)\}dt}{\int_0^{t_{\max}} h_0\{s(t)\}dt}, \quad (2)$$

where

$$h_0(s(t)) = c \exp\left\{ l(\hat{\phi}_0; s(t)) - l(\hat{\phi}(s(t)); s(t)) \right\} |j_{\phi\phi}(\hat{\phi}(s(t)))|^{-1/2} |j_{\lambda\lambda}(\hat{\phi}_0; s(t))|^{1/2},$$

where $\hat{\phi}(s(t))$ is the MLE for the likelihood given in Equation (1).

The upper limit of integration, $t_{\max}$, is obtained by noting that under the original parameterization, the MLEs for tangent exponential family approximation given in Equation (1), for a value of $s(t)$, are

$$\hat{\beta}_i(t) = tX_i/a_i + (1-t)\hat{\beta}_{0,i}, \tag{3}$$

$$\hat{\mu}_i(t) = tY_i/f_i b_i + (1-t)(\hat{\beta}_{0,i} + f_i\hat{\mu}_{0,i})/f_i - \hat{\beta}_i(t)/f_i, \tag{4}$$

and the fact that these estimates need to be positive. Define the sets $D_1 := \{i \in (1, \ldots, n) : \hat{\mu}_{0,i} f_i - Y_i/b_i + X_i/a_i > 0\}$ and $D_2 := \{j \in (1, \ldots, n) : \hat{\beta}_{0,j} - X_j/a_j > 0\}$ the maximum value that t can take is

$$t_{\max} = \min\left[\min_{i \in D_1} \left\{ \frac{f_i\hat{\mu}_{0,i}}{f_i\hat{\mu}_{0,i} - Y_i/b_i + X_i/a_i} \right\}, \min_{j \in D_2} \left\{ \frac{\hat{\beta}_{0,j}}{\hat{\beta}_{0,j} - X_j/a_j} \right\} \right].$$

Finally the information terms are given by:

$$
\begin{aligned}
|j_{\phi\phi}(\hat{\phi}(s(t)))| &= \prod_{i=1}^{n} a_i b_i \hat{\beta}_i(t)(f_i\hat{\mu}_i(t) + \hat{\beta}_i(t)), \\
|j_{\lambda\lambda}(\hat{\phi}_0; s(t))| &= f_1^2 \left\{ \frac{tY_1 + (1-t)b_1(\hat{\beta}_{0,1} + f_i\hat{\mu}_{0,1})}{(f_i\hat{\mu}_{0,1} + \hat{\beta}_{0,1})^2} \right\} \left\{ \frac{tX_1 + (1-t)a_1\hat{\beta}_{0,1}}{\hat{\beta}_{0,1}^2} \right\} \\
&\quad \times \prod_{i=2}^{n} \left\{ \frac{tY_i + (1-t)b_i(\hat{\beta}_{0,i} + f_i\hat{\mu}_{0,i})}{(f_i\hat{\mu}_{0,i} + \hat{\beta}_{0,i})^2} + \frac{tX_i + (1-t)a_i\hat{\beta}_{0,i}}{\hat{\beta}_{0,i}^2} \right\},
\end{aligned}
$$

where $\hat{\beta}_i(t)$ and $\hat{\mu}_i(t)$ are defined in Equations (3) and (4). The p-value is obtained by numerically integrating the numerator and denominator of Equation (2). In our simulation studies, we observe that the test is accurate for $n \leq 16$, however beyond this point the test begins to be anti-conservative under the null.

Source Characteristics We have examined the importance of several source and region characteristics and their relation to the distribution of single-region *p*-values. The full list of characteristics examined is given in Extended Data Table2, and individual jet (or region) characteristics for our sample are given in the Supplemental Information Tables. Here we briefly describe the various classifications and how they were determined.

The 'spectral type' of each source refers to the presence and/or width of the optical/UV emission lines of the AGN nucleus. In general, 'broad-lined' AGN are those with full-width-half-max widths of $\sim$1000 km/s or more, while narrow-line AGN have line widths on the order of a few 100 km/s; it is thought that in most AGN this difference reflects a difference in the level of accretion activity and ionizing continuum, with broad-lined sources showing higher levels of both.

In some sources, no lines at all are detected – such sources are often typed in the literature as 'BL Lac' objects, and these we have grouped with the narrow-lined (lower activity) sources. Spectral type was determined through a search of the literature or, where necessary, by examining archival spectra. For two sources, no optical/UV spectra or previous classification in the literature was available.

The kinetic power carried by the jet ('jet power') was estimated from the monochromatic observed luminosity (as νL_ν) of the extended radio emission at a rest-frame wavelength of 300 MHz. Values were taken from a recent catalogue by Keenan et al.[10], or else determined using the same method and data taken from NED. The redshifts of all sources are known and were taken from NED and/or SIMBAD. The jet angles to the line-of-sight (θ) are estimates taken from the ATLAS-X catalogue[2].

For the observed jet length we simply measured in arcseconds the length from the core position to the end of the jet, following the emission along any bends as necessary. Similarly, for each knot region we measure the distance from the core along the jet in arcseconds. Knot sequence ('knot number') simply refers to the numeric order that the knot appears from the core, in cases with more than one.

The jet classification is taken from the XJET database, where sources are grouped as core-dominated quasars (CDQ, 22 sources), lobe-dominated quasars (10 sources), quasars (2 sources), Fanaroff-Riley type I (FR I, 5 sources) and FR II (15 sources). Here the 'core-dominated quasar' definition is indicative of radio morphology (indicating a very strong radio core) and should not be

confused with the optical spectral type (where quasar would usually suggest broad emission lines).

The average source counts simply reports the total counts (minus estimated background contribution) in the source region. Background/Source count ratio ($\langle n_{\rm src}/n_{\rm bg}\rangle$) is the ratio of estimated background counts in the source region to that of the source region (minus estimated background), averaged over all epochs. A break at approximately 10% roughly divides the sample in two.

Data and Code Availability Statement All observations used in this study are publicly available. We also include extensive tables of reduced data necessary to repeat these analyses as excel files, further described in Supplemental Information. All codes are either publicly available or available by request.

1. Mossman, A., Stohlman, O., Cheung, T., Harris, D. E. & Massaro, F. (2015). URL `https://hea-www.harvard.edu/XJET/`.

2. Reddy, K., Georganopoulos, M. & Meyer, E. ATLAS-X. *arXiv e-prints* (2022).

3. Garmire, G. P., Bautz, M. W., Ford, P. G., Nousek, J. A. & Ricker, J., George R. Advanced CCD imaging spectrometer (ACIS) instrument on the Chandra X-ray Observatory. In Truemper, J. E. & Tananbaum, H. D. (eds.) *X-Ray and Gamma-Ray Telescopes and Instruments for Astronomy.*, vol. 4851 of *Society of Photo-Optical Instrumentation Engineers (SPIE) Conference Series*, 28–44 (2003).

4. Fruscione, A. *et al.* CIAO: Chandra's data analysis system. In Silva, D. R. & Doxsey, R. E. (eds.) *Society of Photo-Optical Instrumentation Engineers (SPIE) Conference Series*,

vol. 6270 of *Society of Photo-Optical Instrumentation Engineers (SPIE) Conference Series*, 62701V (2006).

5. URL https://heasarc.gsfc.nasa.gov/docs/heasarc/caldb/caldb$_intro.html$.

6. McMullin, J. P., Waters, B., Schiebel, D., Young, W. & Golap, K. CASA Architecture and Applications. In Shaw, R. A., Hill, F. & Bell, D. J. (eds.) *Astronomical Data Analysis Software and Systems XVI*, vol. 376 of *Astronomical Society of the Pacific Conference Series*, 127 (2007).

7. URL https://ned.ipac.caltech.edu/.

8. HI4PI Collaboration *et al.* HI4PI: A full-sky H I survey based on EBHIS and GASS. *Astronomy Astrophysics* **594**, A116 (2016). 1610.06175.

9. Fraser, D. A. S., Reid, N. & Sartori, N. Accurate directional inference for vector parameters. *Biometrika* **103**, 625–639 (2016).

10. Keenan, M., Meyer, E. T., Georganopoulos, M., Reddy, K. & French, O. J. The relativistic jet dichotomy and the end of the blazar sequence. *Monthly Notices of the Royal Astronomical Society* **505**, 4726–4745 (2021). 2007.12661.

Acknowledgements E.T.M. acknowledges Chandra Archival Grant 16700615, ADAP grant NNX15AE55G, and NSF grant 1714380. YT and NR acknowledge support from the Natural Sciences and Engineering Research Council of Canada.

This research was made possible through use of data obtained from the Chandra Data Archive and the Chandra Source Catalog, and software provided by the Chandra X-ray Center (CXC) in the application packages `CIAO` and `sherpa`.

The Australia Telescope Compact Array is part of the Australia Telescope National Facility (grid.421683.a) which is funded by the Australian Government for operation as a National Facility managed by CSIRO. We acknowledge the Gomeroi people as the traditional owners of the Observatory site.

This paper makes use of the following ALMA data: ADS/JAO.ALMA#2012.1.00688.S, ADS/JAO.ALMA#2016.1.01481.S. ALMA is a partnership of ESO (representing its member states), NSF (USA) and NINS (Japan), together with NRC (Canada), MOST and ASIAA (Taiwan), and KASI (Republic of Korea), in cooperation with the Republic of Chile. The Joint ALMA Observatory is operated by ESO, AUI/NRAO and NAOJ. The National Radio Astronomy Observatory is a facility of the National Science Foundation operated under cooperative agreement by Associated Universities, Inc.

Author Contributions ETM conceived the project, developed the data analysis methods, contributed to the multi-wavelength data analysis, and wrote the article. AIS carried out the X-ray data analysis with contributions from ETM, KR, PB, ND, DC, and MT. YT and NR contributed the statistical analysis methods and expertise. KR and PB contributed to the data analysis and interpretation. MG contributed to the interpretation and theoretical implications. All authors contributed to the editing of the manuscript and interpretation of results.

Competing Interests The authors declare that they have no competing financial interests.

Additional Information Supplementary Methods, Tables, and Figures are included in the online version of this article. Correspondence and requests for materials should be addressed to E.T.M. (email:

meyer@umbc.edu).

Extended Data Figures and Table

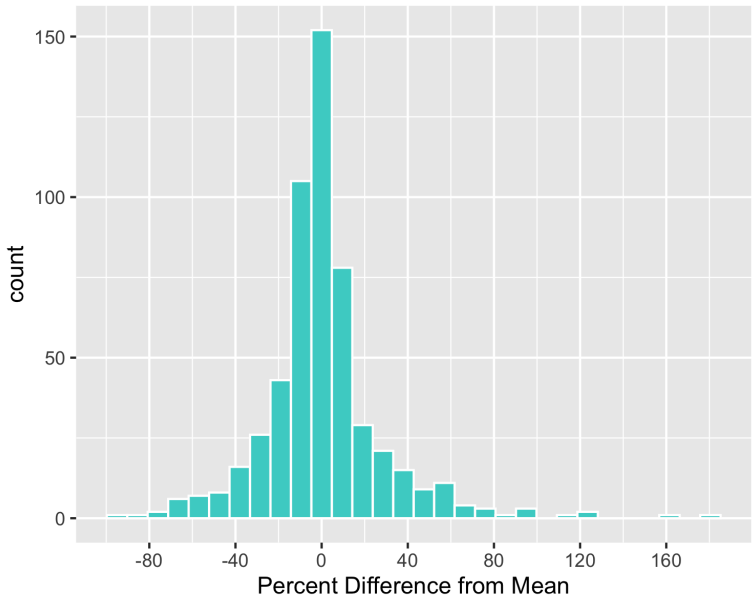

Figure 4 | (Extended Data Figure) **Histogram of the percent difference of each epoch source rate from $\bar{\mu}$ for all regions** Including all epochs on all regions, there are 545 distinct observations. The distribution has a mean of 1.02% and a standard deviation of 28.5%. The mean of the absolute value of the percent difference is 18%.

Table 2 | Extended Data Table - Full results of sub-sample KS-tests against the $U(0,1)$ distribution

Characteristic	Subset	n	Break	KS-test $p-$value	Percentile
Jet Angle	High	78	$\theta >= 15.5^\circ$	0.0001212	6.17
	Low	77	$\theta < 15.5^\circ$	0.1227422	
Average Src. Counts	Many	89	$n > 40$	0.0019570	
	Few	66	$n < 40$	0.0467632	
Background/Source Count ratio	Low	66	$\langle n_{\rm src}/n_{\rm bg}\rangle < 0.1$	0.0010641	
	High	89	$\langle n_{\rm src}/n_{\rm bg}\rangle > 0.1$	0.0246957	
Core dist.	Far	83	$d > 5'$	0.0000327	2.22
	Near	72	$d < 55'$	0.2920501	
Jet Length	Long	82	$\ell > 10'$	0.0008115	
	Short	73	$\ell < 10'$	0.0431792	
Knot Sequence	Later knots	102	...	0.0023121	
	First knots	53	...	0.0208292	
Knot Type	non-hotspot	110	...	0.0025399	
	hotspot	45	...	0.0076676	
Radio Power	Low-Power	51	$L_{300\,\rm MHz} < 10^{43}\,{\rm erg\,s^{-1}}$	0.0012069	
	High-Power	95	$L_{300\,\rm MHz} > 10^{43}\,{\rm erg\,s^{-1}}$	0.1019381	
Spectral Type	Broad-lined	111	...	0.0008109	
	Narrow-lined	33	...	0.4180435	
Redshift	Low	75	$z < 0.6$	0.0000035	0.36
	High	80	$z > 0.6$	0.2296055	
Jet Class	not CDQ	81	...	0.0001501	7.33
	CDQ	74	...	0.1272601	
Jet Class + redshift	not high-z CDQ	100		0.0000032	0.21
	high-z CDQ	55	($z > 0.6$ + CDQ)	0.7034346	

Table 3 | Radio Observations

Object	Date Obs. (YYYY-MM-DD)	Telescope	Project Code	Freq (GHz)	Image Source	Beamsize (Major x Minor)
J0016+7916	1999−08−01	VLA	AP0380	8.46	a	0.25”x0.21”
J0020+1540	2015−06−19	EVLA	15A−357	15	a	0.15”x0.12”
J0037−0109	1990−05−25	VLA	AB0534	8.35	a	0.35”x0.26”
J0057+3021	1996−11−02	VLA	AC0476	4.86	a	0.42”x0.38”
J0108+0135	1989−01−02	VLA	AF170	4.86	c	0.49”x0.44”
J0210−5101	2002−02−01	ATCA	C890	8.64	b	1.33”x1.21”
J0237+2848	1987−08−09	VLA	AG0249	4.84	c	0.45”x0.39”
J0418+3801	2015−03−06	EVLA	15A−164	5.53	a	0.99”x0.88”
J0607−0834	1997−01−06	VLA	AR277	8.46	a	0.33”x0.22”
J0635−7516	1999−08−19	ATCA	VSOP	8.64	b	0.88”x0.88”
J0655+5408	1995−08−06	VLA	AP315	8.06	d	0.35”x0.25”
J0804+1015	2004−09−18	VLA	AB1093	8.46	c	0.25”x0.23”
J0840+2949	1982−02−27	VLA	VAN	4.87	a	0.55”x0.42”
J0922−3959	1998−05−19	VLA	AH0640	8.46	a	0.88”x0.21”
J0947+0725	1999−07−10	VLA	AS659	1.44	a	2.55”x1.48”
J0950+1419	2003−08−18	VLA	AS764	4.71	c	0.41”x0.40”
J1001+5553	1983−11−01	VLA	AB263	4.86	a	1.04”x0.54”
J1007+1248	1991−11−13	VLA	AW249	8.26	c	0.79”x0.65”
J1033−3601	2004−05−12	ATCA	C890	18.9	a	0.88”x0.47”
J1048−1909	1996−12−13	VLA	AL634	8.41	c	0.50”x0.25”
J1058+1951	1986−06−01	VLA	VH0025	4.99	a	0.75”x0.69”
J1130−1449	2001−02−07	VLA	AH730	8.46	b	0.78”x0.58”
J1139−1350	2007−06−23	VLA	AH0938	4.86	a	0.51”x0.43”
J1153+4931	2016−12−07	EVLA	16B−189	15	a	0.12”x0.11”
J1205−2634	1988−10−30	VLA	AE0059	4.86	a	0.92”x0.36”
J1219+0549	1986−11−26	VLA	AB412	1.49	c	18.00”x18.00”
J1220+3343	1986−04−27	VLA	AL119	4.86	c	0.36”x0.34”
J1229+0203	1990−05−10	VLA	AP0001	8.43	a	0.39”x0.23”
J1232−0224	1994−03−21	VLA	AK353	8.35	a	0.28”x0.27”
J1352+3126	2000−12−15	VLA	AT249	4.86	c	0.33”x0.27”
J1357+1919	2016−10−22	ALMA	2016.1.01481.S	97.5	a	0.77”x0.53”
J1406+3411	1987−10−11	VLA	AM224	4.76	a	0.46”x0.39”
J1421+4144	1993−11−21	MERLIN2	–	1.53	d	0.13”x0.13”
J1421−0643	2016−09−24	ALMA	2016.1.01481.S	97.5	a	0.37”x0.29”
J1424−4913	2013−12−14	ALMA	2012.1.00688.S	239.42	a	1.48”x0.73”
J1449+6316	1993−09−24	MERLIN2	–	1.42	d	0.15”x0.15”
J1512−0905	1986−05−06	VLA	AO0070	4.86	a	0.51”x0.39”
J1549+6241	1991−07−20	VLA	AF213	4.86	c	0.39”x0.38”
J1606+0000	1984−12−17	VLA	AH176	4.86	a	0.50”x0.50”
J1642+3948	1985−01−31	VLA	AC120	4.86	b	0.45”x0.45”
J1642+6856	2015−06−22	EVLA	15A−357	15	a	0.16”x0.11”
J1704+6044	1982−11−03	VLA	LAIN	1.42	d	1.85”x1.85”
J1720−0058	1996−12−01	VLA	BS0043	1.66	a	1.69”x1.33”
J1806+6949	1988−11−25	VLA	AR0168	8.44	a	0.34”x0.21”
J1849+6705	2016−09−01	EVLA	16B−386	9.99	c	0.77”x0.55”
J1927+7358	1983−10−31	VLA	AE27	4.86	a	0.47”x0.35”
J1959+4044	1984−01−14	VLA	PERLEY	4.53	b	0.40”x0.40”
J2042+7508	1998−12−04	VLA	AR0386	4.86	a	5.59”x4.71”
J2105−4848	2004−05−10	ATCA	C890	17.7	a	0.79”x0.54”
J2157−6941	2013−10−30	ATCA	C2034	18	a	0.55”x0.47”
J2158−1501	1996−10−29	VLA	AG0499	8.46	a	0.34”x0.23”
J2218−0335	2004−11−21	VLA	AL0634	1.4	c	1.66”x1.33”
J2223−0206	1996−11−25	VLA	AP337	8.46	c	0.27”x0.23”
J2253+1608	2002−04−14	VLA	BR0080	8.41	a	0.25”x0.23”

[a] Data reduced for this paper, [b] Taken from XJET database,
[c] Taken from NVAS cutout archive, [d] Taken from NED

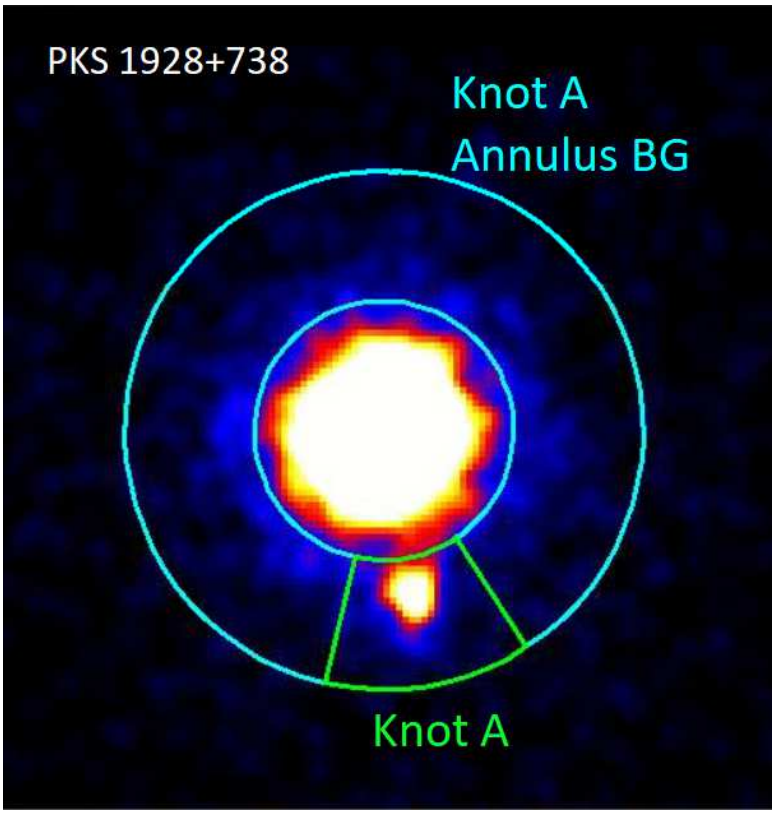

Figure 5 | (Extended Data Figure) **Example of an annulus-style background region.** Shown is the merged sub-pixel *Chandra* X-ray image of the core-dominated quasar PKS 1928+738. Our region-of-interest for this source is knot A, outlined by the green region. Due to the proximity of the knot to the core, we use an annulus background region, outlined in cyan, to account for the core contribution to the background in the knot A region.

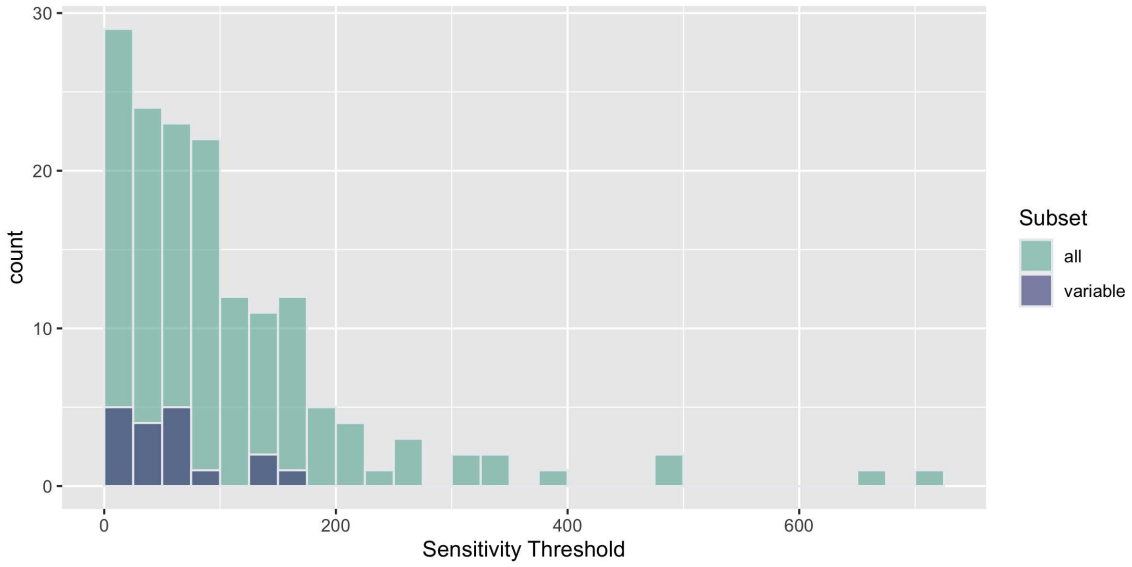

Figure 6 | (Extended Data Figure) **The green histogram shows the maximum ST values (as a percentage relative to $\bar{\mu}$).** The subset of regions with single-region p-values less than 0.05 are shown in blue.

Supplemental Information

Sensitivity Threshold Analysis The analysis here is complicated due to being a completely archival study, with no standardization in observing cadence or depth of observations. It is useful to examine the effect of the observation characteristics on our results. In particular, we have defined a metric which we call the sensitivity threshold or ST, which is designed to roughly capture the level of variability we can detect for any given region given the actual observations of it in our study.

The ST is calculated beginning with the source and background exposure values and photon counts for all observations of a given region. This data is analysed normally through our likelihood analysis. If the test returns $p > .05$ that the intrinsic source flux is steady, then we artificially increase the source photon counts recorded in the first observation by 1. We then rerun our new data through the likelihood analysis. We repeat this process until the model returns $p < .05$. At this point, we calculate the percent difference for each observation relative to the MLE flux value after adjusting the photon counts.

The photon counts for this observation are then reset. We subtract 1 photon count and recalculate the *p*-value. We again repeat this process until the model returns $p < .05$ or until subtracting further counts would reduce the photon counts for the observation to 0 or would result in a source region flux less than the background flux. If the model returns the requisite *p*-value first, we again record the percent difference for each observation relative to the MLE flux.

This process of adding and subtracting counts to lower the *p*-value is repeated for each ob-

servation for a given knot. Once this is completed, we take the maxima and minima of the percent differences for the knot. These two values define our sensitivity threshold (ST)

In cases where the p-value returned by our initial likelihood test is less than .05, we perform this procedure in reverse, increasing or decreasing the counts until the test returns a p-value greater than .05. We then calculate the percent differences and ST using these counts values.

In essence, these numbers define the percent change in flux, negative and positive, that would be necessary for our test to return a single-region p-value $< .05$. Above all else, this metric demonstrates the limitations of our study. The median values for the ST higher and lower limits are 82.7% and -47.5%. This means that for half of the knots in our sample, we are not sensitive to tens-of-percent variability from the mean, and these regions would only be noted as variable if they underwent relatively large changes of a factor of 2 or more.

Extended Data Figure 6 shows a histogram of ST for our analysis sample in green. The subset of regions which appear variable (single-region p-values < 0.05) are shown as the blue histogram. As expected, most of these have relatively low positive ST values.

Supplemental Tables

Four supplemental tables giving the full sample description and all measurements required for repeating the analysis are included as excel files. We here describe their content.

Table 1 describes the characteristics of our sample of 55 jets (our main sample plus 3C 305

and 3C171 for completeness). The columns are (1) IAU name, (2) Common name, (3) jet classification, (4) J2000 right ascension in HH:MM:SS, (5) J2000 declination in DD:MM:SS, (6) redshift, (7) estimated jet angle in degrees, (8) the number of distinct jet features analysed, (9) the number of distinct *Chandra* observations (epochs), (10) the maximum and minimum time separation between observations, (11) the Cosmology-corrected angular size scale (in kpc/″), (12) the galactic Hydrogen column density value used (in units of 10^{22} cm^{-2}), and (13) the total observed jet length in arcseconds and (14) the same in kiloparsecs.

Table 2 describes the characteristics of each *Chandra* observation. There is one row for each epoch, for a total of 183 rows. The columns include (1) the IAU name of the target source, (2) the *Chandra* observation ID number, (3) the decimal date of the observation, (4) a flag column for readout streak correction, (5) the initial total exposure time, and (6) the total observing time in ks after removing background flares.

Table 3 describes the characteristics of all 155 analysis regions, as well as the 'total jet' regions for jets with more than one knot, for a total of 200 rows. The columns are (1) the IAU name of the source, (2) the region name, (3) the type of background region used – annulus (ANN) or generic (GEN), (4) the total counts in the region over all observations, (5) the background model or treatment used for the spectral fit, (6) the knot area in ACIS pixels, (7) the knot area in arcseconds squared, (8) the flux normalisation of the region SHERPA fit, (9) the spectral index from the region SHERPA fit, (10) the single-region p-value from the Poisson model, (11) the estimated mean source rate $\bar{\mu}$ in cts s^{-1} cm^{-2}, and (11) the upper and (12) lower sensitivity threshold (ST, see

supplemental information) for each knot.

Table 4 gives details specific to a particular knot and epoch of observation, a total of 556 rows. Columns are (1) the IAU name of the source (2) the region name, (3) the *Chandra* observation ID number, (4) the source region exposure in ks, (5) the background exposure in ks, (6) the source region counts, (7) the background region counts, (8) the encircled counts fraction and (9) the estimated source flux in cts s^{-1} cm^{-2}.